nature communications

Article

https://doi.org/10.1038/s41467-025-64797-x

Interfacial oxidation of boron proceeds through a stable B_6O intermediate

Received: 8 April 2025

Accepted: 25 September 2025

Published online: 06 November 2025

Check for updates

Jian Wang[1,2], Kai Zhong[2], Xinxing Zeng[2], Yaofeng Mao[1], Jie Chen[2], Fude Nie[2], Huiyang Gou[3] ✉ & Jun Wang[1] ✉

The oxidation of boron (B) is of great significance in catalysis, metallurgy, corrosion, and combustion. However, understanding the early stages of oxidation and identifying intermediate phases remain a long-standing challenge. Here we reveal an oxidation mechanism termed the W–J model; unlike classical models that rely on the diffusion of oxygen or boron through a B_2O_3 layer, the initial reaction in the W–J model takes place at the interface between the boron core and the B_2O_3 shell. This interfacial reaction produces an oxidized intermediate, B_6O, which is then further oxidized to form B_2O_3. The formation of B_6O plays a crucial role in regulating the oxidation process. Its high thermal stability and strong oxygen affinity act as barriers to continuous oxidation, thereby lowering the ignition and combustion efficiency of boron. These findings highlight a fundamentally different reaction pathway that may help explain the limited reactivity observed in practical applications.

Elemental boron (B) exhibits exceptional mechanical, electrical, and chemical properties[1–3] and diverse applications, including catalysis[4,5], capacitors[6,7], metallurgy[8], and microelectromechanical systems[9], as well as being the highest calorific value fuel for energy storage and release[10–13]. The B oxidation is critical to the deactivation of B-based catalysts and capacitors, and the energy release rate in high-energy fuel systems is closely tied to the oxidation pathway. Thus, extensive research has focused on understanding the oxidation reaction mechanism to improve the stability, longevity, and ignition and combustion efficiency of solid rocket motors. Generally, the B_2O_3 shell on B particles, with a low melting point (723 K) and a high boiling point (2133 K), remains intact during the oxidation process[10,14,15]. Additionally, Marangoni convection[16–18] contributes to the self-healing of the B_2O_3 layer, complicating its removal. Therefore, a thorough understanding of the oxidation reaction mechanism of B requires investigating the interface between B and B_2O_3 during the ignition and combustion processes.

Currently, two classical models describe the interfacial reaction between B and B_2O_3: the King model[14,19,20] and the L-W model[21]. The King model proposes that oxygen (O_2) diffuses into B_2O_3 layer and reacts with internal B. Experimental observations by Dreizin et al.[22] confirmed the diffusion of O_2 within the B_2O_3 layer; however, the compact, glassy nature of B_2O_3 at elevated temperatures hinders this process. Additionally, the highly oxidized state of B_2O_3 impedes efficient oxygen transfer. In contrast, the L-W model suggests that B diffuses outward through B_2O_3 layer, reacting with external O_2, generating the intermediate polymer $(BO)_n$, which then infiltrates the B_2O_3 shell and reacts with O_2. Theoretical work by Glassman et al.[23] indicates that solubility of B in liquid oxides exceeds that of O_2, while investigation by Yeh et al.[24,25] shows that the diffusion rate of $(BO)_n$ is significantly higher than that of O_2 at elevated temperatures. The L-W model emphasizes the formation and oxidation of the $(BO)_n$ intermediate as key to the interfacial reaction. However, there remains an insufficiency of experimental and theoretical data to fully characterize the creation process and unique structure of $(BO)_n$. Furthermore, inconsistencies between the King and L-W models highlight unresolved issues in understanding the underlying causes of B's low ignition and combustion efficiency.

In this study, to explore the oxidation mechanism of B and identify intermediate species, three reaction interfacial models of B-B_2O_3, B-B_2O_3-O_2, and B-O_2 are developed (Fig. 1). The fluorine-containing rubber F14, known for its excellent mechanical strength, chemical stability, and corrosion resistance, was used as a surface coating

[1]School of Mechatronical Engineering, Beijing Institute of Technology, Beijing, China. [2]Institute of Chemical Materials, China Academy of Engineering Physics, Mianyang, China. [3]Center for High Pressure Science and Technology Advanced Research, Beijing, China. ✉e-mail: huiyang.gou@hpstar.ac.cn; wjun927@bit.edu.cn

https://doi.org/10.1038/s41467-025-64797-x

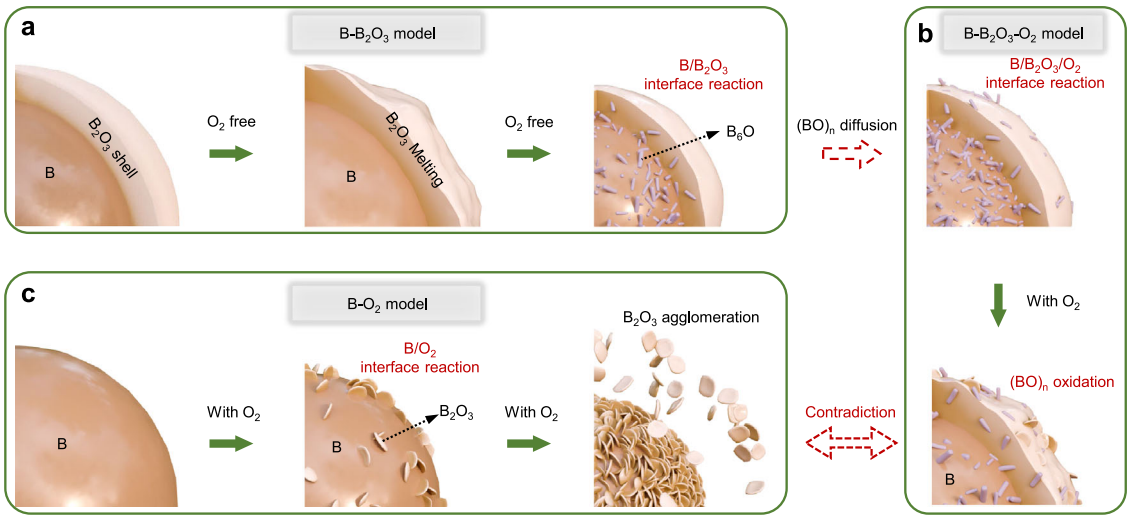

Fig. 1 | Schematic diagram of the research roadmap. The oxidation mechanism of boron was elucidated through the examination of three interfacial reaction processes using three distinct models. **a Model 1:** The B-B_2O_3 model was developed by introducing boron into an argon environment, and the chemical pathway at the B/B_2O_3 interface was examined. **b Model 2**: The B-B_2O_3-O_2 model was developed by introducing boron into the air atmosphere, and the chemical process at the B/B_2O_3/O_2 interface was examined. **c Model 3**: The fluoropolymer-modified boron (B@F) was subjected to an air environment to establish a B-O_2 model, and the chemical process at the B/O_2 interface was investigated.

material. Through surface etching, it enabled the controlled construction of the B–O_2 reaction interface (B@F). The formation and structure of the intermediate $(BO)_n$ were systematically investigated by advanced imaging and spectroscopic techniques. Simultaneously, molecular dynamics simulations are employed to study the interface reaction of these models between B and B_2O_3. The results reveal that the initial reaction occurs on the interface between B core and B_2O_3 shell, leading to the formation of B_6O, which is subsequently oxidized by O_2 to produce B_2O_3. The B_6O intermediate acts as a barrier, hindering further oxidation of B and resulting in reduced ignition and combustion efficiency.

Results and Discussion

The formation mechanism of intermediate B_6O

The initial construction of a B-B_2O_3 reaction interface is introduced to investigate the interaction between B and B_2O_3 in the B-B_2O_3 model. Amorphous boron, with its native B_2O_3 shell, was heat-treated in argon at various temperatures to elucidate the interfacial reaction process. X-ray diffraction (XRD) patterns in Fig. 2a reveal the primary phases of B (PDF#31-0207), B_2O_3 (PDF#06-0297), and B_6O (PDF#50-1505) prior to heat treatment. As the calcination temperature increases, the intensity of the B_2O_3 diffraction peaks gradually decrease, while the B_6O peaks increase. Notably, no B_2O_3 diffraction peaks are observed at 1400 °C, suggesting that B_2O_3 may become amorphous and undetectable by XRD once the temperature exceeds its melting point (450 °C). Additionally, chemical reactions on the interface between B core and B_2O_3 shell likely contribute to the reduction of B_2O_3 and the formation of B_6O. X-ray photoelectron spectroscopy (XPS) spectra (Fig. S1) further confirm the results found in XRD, showing a significant decrease in the proportions of B_2O_3 (from 7.04% to 6.41%) and B (from 72.06% to 54.04%), while the concentration of B_6O increases from 25.50% to 39.55%. These results demonstrate that the B/B_2O_3 interface reacts to form B_6O (Eq. (1)), leading to a decrease in B_2O_3 and an increase in B_6O when B is heated in an oxygen-free environment. Equation (1) represents this process.

$$16B(s) + B_2O_3(s, l) \rightarrow 3B_6O(s, l) \quad (1)$$

Given the minimal presence of the native oxide layer on the B surface, B/B_2O_3 composites were synthesized based on the stoichiometric ratio outlined in Eq. (1). The morphology and structure of these composites after high-temperature heat treatment were investigated to better understand the interfacial reaction between B and B_2O_3. XRD data (Fig. S2a) reveal that prior to calcination, the main phases are B and $B(OH)_3$, which forms through the hydrolysis of B_2O_3. After calcination, the primary phase transitions to B_6O, with XPS analysis (Fig. S2b) showing the disappearance of B and B_2O_3 peaks, replaced by distinct B_6O peaks. While recent reports[26–29] suggest that B_6O forms during the combustion of B, attributing its generation to incomplete combustion, these studies fail to address the specific process and role of B_6O in B oxidation.

High-resolution transmission electron microscopy (HRTEM) images (Fig. 2b) of the B/B_2O_3 composites before and after the reaction show a uniformly adherent, dense amorphous B_2O_3 layer on the surface of the B crystals. The diffraction pattern from the Fourier transformation of the region marked by the yellow box is shown in the inset. The differences in HRTEM images and diffraction spots suggest that a reaction occurred on the interface between B core and B_2O_3 shell, leading to the formation of a new compound upon calcination. The angles between the (012) and (003) planes, and between the (101) and (003) planes, were measured to be 55° and 69°, respectively. These values are in close agreement with those from the XRD standard card and the single-crystal structure of B_6O, which report angles of 52.87° and 69.26°, respectively. After the reaction, both B and B_2O_3 are absent, confirming that B_6O forms directly from the interaction of B and B_2O_3. Our results suggest that B_6O is formed at the B/B_2O_3 interface, not as a result of incomplete oxidation, supporting the hypothesis that B_6O could be a potential structure for the $(BO)_n$ intermediate proposed in the King and L-W models.

The investigation into the role of B_6O in the ignition and combustion processes of B was carried out by constructing the B/B_2O_3/O interface, as indicated by the results above. In this context, the native B_2O_3 oxide layer on the surface of amorphous B was utilized, and B was subjected to heat treatment in oxygen at varying temperatures to study the interfacial reaction between B, B_2O_3, and O_2. The XRD patterns (Fig. S3a) reveal that, as temperature increases, the diffraction peak corresponding to B diminishes while peaks for B_2O_3 become more prominent. Additionally, heat-treated samples display characteristic peaks for B_6O, with the intensity of these peaks initially increasing before decreasing at higher temperatures. To further

https://doi.org/10.1038/s41467-025-64797-x

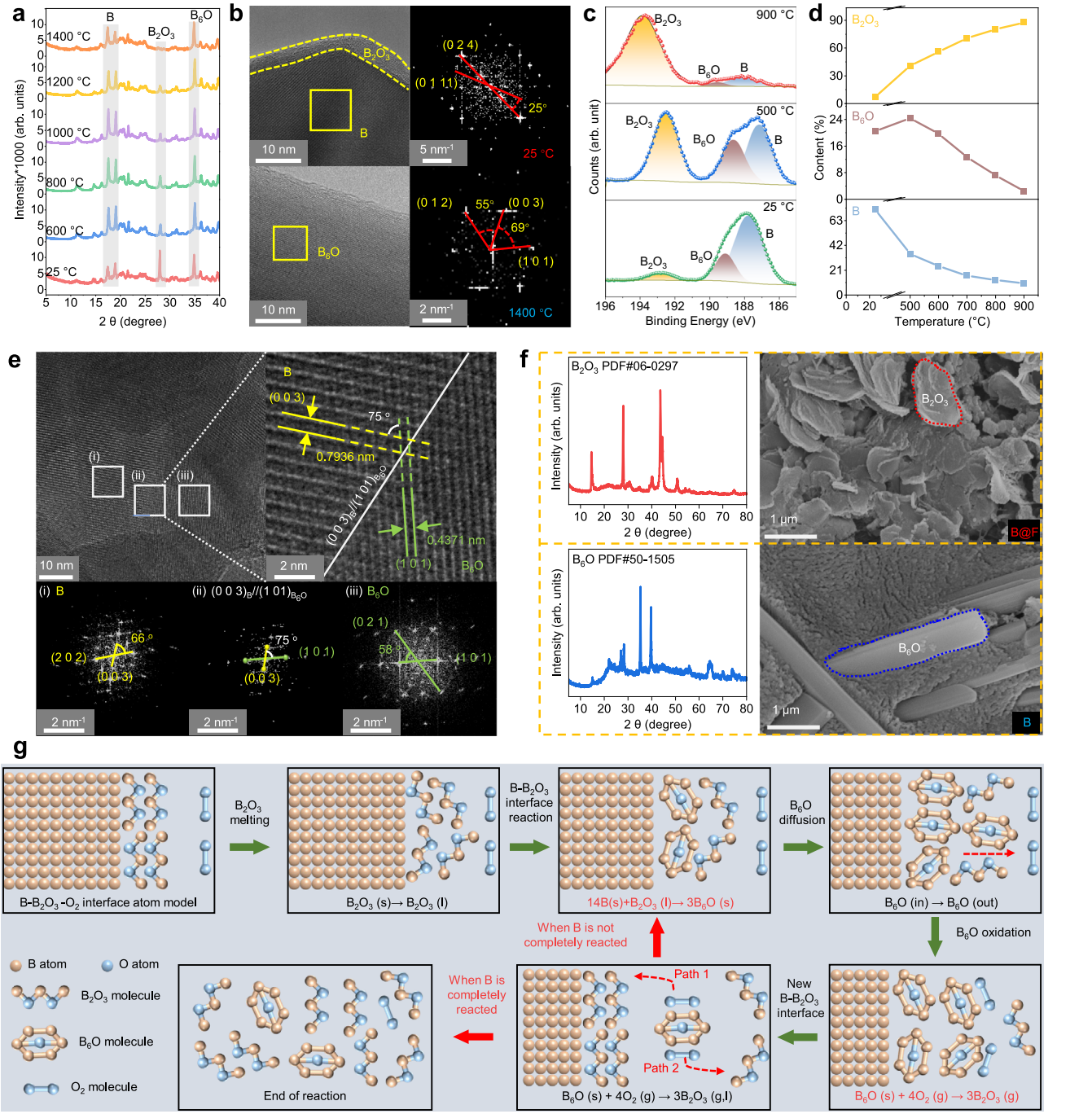

Fig. 2 | The structure and component of boron after calcination in different conditions. a the XRD patterns of boron after calcination in argon at different temperature. **b** representative HRTEM images and DDPs of B/B_2O_3 composites before calcination in argon (top), and representative HRTEM images and DDPs of B_6O obtained from the B/B_2O_3 composites after calcination in argon (bottom). **c** the B *1s* XPS spectra of B after calcination in air at 25 °C, 500 °C, and 900 °C temperature. **d** the percentage of B_2O_3, B_6O and B at different temperature in air according to XPS. **e** Representative HRTEM images of B particle after calcination in air at 500 °C (top left) and detail HRTEM image of B-B_6O interface (top right). DDPs of the small areas marked with (i) and (iii) refer to the B and B_6O, respectively, which are shown at the bottom left and bottom right. The middle panels correspond to the sum of both DDPs. **f** The XRD patterns and SEM images of combustion products of B@F (top) and B (bottom). **g** schematic diagram of the interfacial reaction mechanisms of B and B_2O_3.

characterize the chemical valence states of B, XPS spectra were analyzed, and the relative proportions of B_2O_3, B_6O, and B were quantified by peak area analysis (Figs. 2c, d, Fig. S3b). The data show a progressive increase in B_2O_3 content and a corresponding decrease in B as the temperature rises, while B_6O content initially increases and then decreases. This trend aligns with the XRD results, supporting that B_6O forms as an intermediate product in the interface reaction between B and B_2O_3, facilitating the outward mass transfer of B to the particle surface, where it subsequently reacts with O_2 to form B_2O_3.

HRTEM images of the calcined samples (Fig. 2e) reveal the coexistence of B and B_6O at the nanoscale, particularly at the crystal boundaries within the same crystallites. The exposed (003) crystal plane of B and the (101) crystal plane of B_6O form an angle of 75°. Detailed analysis of the digital diffraction patterns (DDPs) from various regions of the calcined composite indicates that region (i) corresponds

to B, region (iii) to B_6O, and region (ii) to the crystal boundary where diffraction spots of both B and B_6O overlap. This boundary exhibits the (003) plane of B and the (101) plane of B_6O, maintaining the 75° angle. These observations suggest that B_6O forms through the reaction between B and B_2O_3, developing along the (003) crystal plane of B, consistent with previous analyses in B-B_2O_3 model.

Further insights are provided through infrared spectroscopy (Fig. S4) and electron microscopy data (Fig. S5). Upon the formation of B_6O at the B/B_2O_3 interface, B_6O gradually diffuses to the particle surface, where it reacts with O_2 to produce B_2O_3, thus facilitating the reaction between B and O. The chemical process involved can be represented by Eqs. (2) and (3).

$$16B(s) + B_2O_3(s, l) \rightarrow 3B_6O(s, l) \quad (2)$$

$$B_6O(s, l) + 4O_2(g) \rightarrow 3B_2O_3(l, g) \quad (3)$$

The results indicate that B_6O is exclusively formed as the primary reaction product in the presence of B_2O_3, while in its absence, B_2O_3 is the predominant product. Firstly, to establish the reaction interface of B-O_2, B covered with fluoropolymer (B@F) was synthesized, based on the surface etching reaction between F and B_2O_3. The morphologies and particle size distribution of B@F, shown in Fig. S6, confirm its successful preparation. Experiment 4 (Fig. S7) and our previous work[30,31] demonstrates the effective removal of the oxide layer by the fluoropolymer. Then, the above hypothesis is further substantiated by analyzing the combustion products of B and B@F, which were burned in a 1 MPa oxygen environment. XRD patterns in Fig. 2f reveal that the combustion of B predominantly results in B_6O, while B@F combustion yields both B_2O_3 and a small amount of B_6O. XPS spectra in Fig. S8 show a higher proportion of B_6O in the combustion products of B and a greater proportion of B_2O_3 in those of B@F. Further analysis of the surface structures (Fig. 2f and Fig. S9) reveals that B exhibits rod-like structures with a B to O atomic ratio of approximately 6:1, consistent with the presence of B_6O. In contrast, B@F exhibits a flaky structure with a B to O atomic ratio of 2:3, indicating that it primarily consists of B_2O_3.

The fluorine atoms in B@F interact initially with the B_2O_3 shell, exposing the interior active B, which then reacts with O_2 to generate additional B_2O_3. Marangoni convection causes the newly formed B_2O_3 shell to envelop the unreacted B, thus creating a new B/B_2O_3 interface. This results in minimal B_6O formation in B@F. The overall process can be described by Eqs. (4)–(6). These results support the hypothesis that the formation of B_6O is contingent upon the presence of B_2O_3, and they systematically elucidate the reaction mechanism on the interface between B core and B_2O_3 shell (Fig. 1g).

$$B_2O_3(l) + 6CF(g) \rightarrow 2BF_3(g) + 3CO(g) + 3C(s) \quad (4)$$

$$4B(s) + 3O_2(g) \rightarrow 2B_2O_3(s, l) \quad (5)$$

$$16B(s) + B_2O_3(s, l) \rightarrow 3B_6O(s, l) \quad (6)$$

The chemical reactivity of intermediate B_6O

As an intermediate compound in the B-B_2O_3 interface reaction, B_6O significantly influences the combustion and ignition characteristics of B. Notably, the complete oxidation of each mole of B requires three-quarters of a mole of oxygen (Eq. (3)), whereas the complete oxidation of each mole of B_6O consumes four moles of oxygen (Eq. (5)), more than five times the amount required for B. This high oxygen consumption makes B_6O less reaction efficiency. To further assess the combustion reactivity of B_6O, we compare the flame propagation, pressure output, ignition delay time, and thermal processes of B, B@F, and B_6O. B_6O was synthesized by calcining B/B_2O_3 composites under a N_2 atmosphere, as detailed in the preparation of B_6O section. The results show that both B and B@F exhibit a larger flame area and higher light intensity (Fig. 3a, 3b), while B_6O demonstrates reduced combustion reactivity. Pressure output data (Fig. 3c) reveal that B_6O generates gas at a much slower rate (99.9 kPa·s^{-1}) than B (103.9 kPa·s^{-1}) and B@F (2451.5 kPa·s^{-1}), indicating its lower heat release efficiency (Fig. 3d). Furthermore, B_6O exhibits the longest ignition delay time (Fig. 3e), confirming its diminished reactivity and prolonged ignition delay. In conjunction with the findings of section 2.1, it is evident that the concentration of oxidized intermediate in B@F, B, and B_6O samples rises during the early reaction period, which directly accounts for the significant disparity in combustion performance among B@F, B, and B_6O. These findings emphasize the inhibitory effect of B_6O on the ignition and combustion of B particles, in contrast to B@F's role in effectively removing the inert B_2O_3 layer from B's surface, thereby enhancing combustion performance.

The thermal reaction processes of B, B@F and B_6O were analyzed using simultaneous thermal analysis (TG-DSC). DSC curves in Fig. 3f reveal that B@F exhibits the highest heat release and the lowest peak temperature, whereas B_6O shows the smallest heat release and the highest peak temperature. Additionally, TG curves (Fig. 3g) indicate that B_6O has the lowest reaction efficiency. DTG curves in Fig. 3h reflect the reaction rates, indicating that B_6O has the lowest reaction rate compared to B and B@F. Additionally, particle morphologies and components of B@F at various temperatures, shown in Fig. S10-S12, confirm that the reaction efficiency of B@F surpasses that of B across all temperatures. As B@F removes the B_2O_3 shell due to the surface etching of F, the initial reaction of B@F transitions from an interfacial reaction between B core and B_2O_3 shell to a direct reaction between B and O_2, resulting in a reduction of B_6O generated in the reaction process, thereby improving combustion efficiency and rate. These findings align with the results in Fig. 3a-d, further illustrating that B_6O has a highly negative reactivity and oxygen consumption, allowing substantial amounts to form without continually reacting to create B_2O_3 during B combustion.

Reactive molecular dynamics simulations

To gain insights into the atomic-level reaction processes of B, reactive molecular dynamics (RMD) simulations were conducted using four models of B-B_2O_3, B-B_2O_3-O_2, B-O_2, and B_6O-O_2 according to the experiments, as illustrated in Fig. S13a. The simulations utilized a canonical ensemble (NVT) with a Nose-Hoover thermostat and employed the reactive force field (ReaxFF) for H/O/N/B developed by Weismiller et al.[32]. This approach has proven effective in elucidating the oxidation behavior of B particles[18,33,34] (Fig. S13b, c).

The morphological snapshot of the B-B_2O_3 model in Fig. S14 demonstrates that oxygen atoms in the B_2O_3 layer diffuse inward, while boron atoms in the B layer move outward. The oxidation process of B is a critical focus of this study. A representative oxidation pathway for a boron atom at the B-B_2O_3 interface is illustrated in Fig. 4a. As heating occurs, the boron atom in B layer quickly migrates to the surface, resulting in a decrease in B-B bonds to four and then three at 4 ps and 4.4 ps, respectively. At 4.5 ps, the boron atom contacts an oxygen atom in the B_2O_3 layer, forming a B-O bond, and subsequently forms two additional B-O bonds at 5 ps. The number of B–O bonding reaches three at 200 ps and remains constant thereafter. This oxidation state persists throughout the simulation, indicating that the interactions in the B-B_2O_3 model involve chemical reactions rather than mere melting and physical diffusion. Coupled with the unique coordination of B_6O and B_2O_3 shown in Fig. S13b, c, these results suggest that B_6O is produced during the reaction between B and B_2O_3 and progressively diffuses outward, consistent with previous experimental results (Fig. 2a).

https://doi.org/10.1038/s41467-025-64797-x

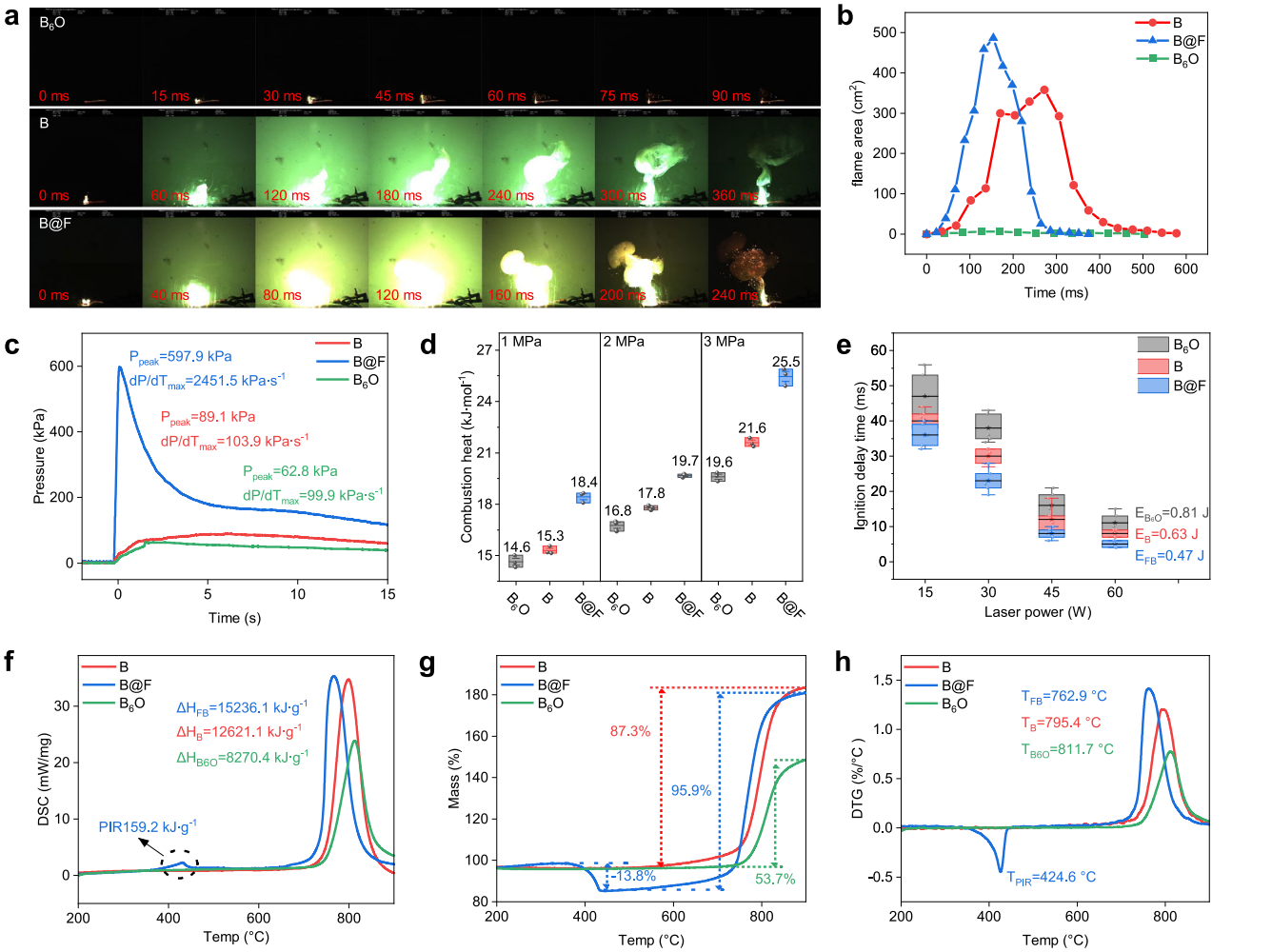

Fig. 3 | The combustion reactivity of B, B@F and B_6O. **a** the flame propagation process in atm air ignited by Ni-Cr wire. **b** the flame area calculated according to flame imagens. **c** the time-dependent pressure evolution curves. **d** the combustion heat in different oxygen pressure. **e** the ignition delay time in different laser power. **f** the thermal reaction process analyzed by DSC curves. **g** the thermal reaction process analyzed by TG curves. **h** the thermal reaction process analyzed by DTG curves.

Figure S15 presents snapshots of the B, B_2O_3, and O_2 layers in the B-B_2O_3-O_2 model under heating. The results reveal the melting of B_2O_3, the outward diffusion of boron atoms from the B layer, and the inward diffusion of oxygen atoms from the O_2 layer. Three boron atoms with the high diffusion displacements at 500 ps are identified as B1, B2, and B3, with their specific oxidation processes illustrated in Fig. 4b. The B1 atom, initially on the surface with three B-B bonds and one B-O bond, experiences a decrease in B-B bonds and an increase in B-O bonds as it diffuses, ultimately forming a structure similar to B_2O_3. The B2 atom starts within the B layer with four B-B bonds and transitions to a B_2O_3-like structure by 240 ps. The B3 atom forms two B–O bonds at 45 ps and ultimately adopts a B_2O_3-like configuration by 92 ps. Furthermore, the radial distribution function (RDF) analyses of the B-B_2O_3 and B-B_2O_3-O_2 models at 500 ps provide additional evidence supporting the formation of B_6O (Fig. S16). In all cases, B initially reacts with B_2O_3 to form a $^{[1]}$B, that is B_6O as the intermediate product. As B_6O diffuses outward and O_2 diffuses inward, B_6O reacts with O_2 to generate a $^{[3]}$B, that is, B_2O_3. We have also simulated the chemical processes in the B_6O-O_2 and B-O_2 models, as detailed in the supplementary material (Fig. S17 and S18). These findings indicate that B_6O progressively oxidizes to form B_2O_3, while elemental B, lacking an oxide layer, directly reacts with O_2 to produce B_2O_3, consistent with previous experimental and simulation results (Fig. 2).

In the crystal structure of B_6O, each oxygen atom forms three B-O bonds with neighboring boron atoms, denoted as $^{[3]}O^{3S}$, which constitutes a key structural feature of the B_6O crystal, as shown in Fig. 4c and Fig. S13c. We analyze the distribution and quantity of the $^{[3]}O$ structures at a 500 ps in various models, as illustrated in Figs. 4d, 4e. In the B-B_2O_3 model, a total of 115 $^{[3]}O$ structures are generated upon heating, with a uniform distribution within the B_2O_3 layer. In the B-B_2O_3-O_2 model, 77 $^{[3]}O$ structures are predominantly located in the molten B_2O_3 region. Conversely, the B-O_2 model shows minimal formation of the $^{[3]}O$ structure, with only 15 instances observed. These results indicate that B_6O primarily forms at the interface between B and B_2O_3, with higher quantities of B_2O_3 correlating to increased B_6O formation.

Combined with the experimental results, it can be concluded that B_6O functions both as an intermediate in the oxidation of B, facilitating mass transfer between internal B and external O, and as an interface barrier that limits the chemical reactivity of B. B_6O is initially formed at the B-B_2O_3 interface through the chemical reaction between B and B_2O_3. It then diffuses to the surface of the B particles, where it reacts with O_2 to generate B_2O_3 as the oxidation process continues. This reaction mechanism is referred to as the W-J model in this study. However, the high oxygen consumption and low reactivity of B_6O hinder its oxidation, resulting in prolonged ignition delays and reduced combustion efficiency.

https://doi.org/10.1038/s41467-025-64797-x

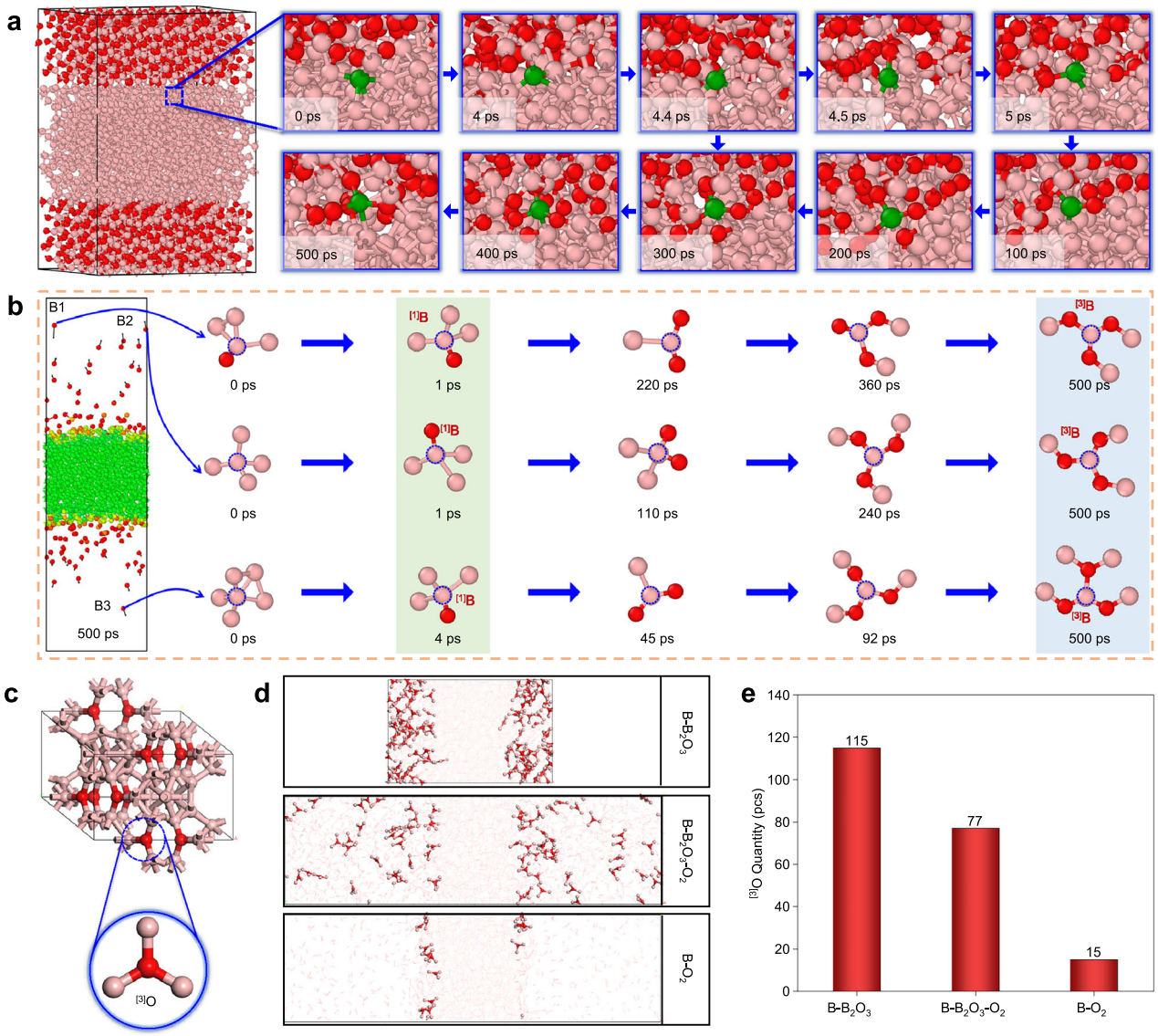

Fig. 4 | The simulation results for different layered models (the red spheres represent O atoms; the pink spheres represent B atoms). a oxidation process of a B atom (shown in green for clarity) in the B-B_2O_3 model. **b** the oxidation process of marked B atoms in the B-B_2O_3-O_2 model. **c** $^{[3]}O$ structure in the B_6O crystal. **d** $^{[3]}O$ structure in different models at 500 ps (The bright red sphere represents $^{[3]}O$ structure). **e** $^{[3]}O$ structure quantity in different models at 500 ps.

In summary, an interfacial reaction mechanism called W-J model, is systematically investigated at the macro and atomic scales based on experiments and RMD simulations. The results propose that the compound boron suboxide (B_6O) as an intermediate resulted from the interfacial reaction between the B core and B_2O_3 shell. The negative reactivity and high oxygen consumption of B_6O pose a notable challenge in its further oxidation to B_2O_3, therefore greatly impeding the ignition and combustion performance of B. The oxidation mechanism of B is empirically researched and can be utilized in the fields of aerospace, microelectromechanical systems, and civic sectors.

Methods

Materials

Boron particle was purchased from Zhong Nuo New Materials with an average size of 5 μm. F14 was obtained from the Institute of Chemical Materials, CAEP (Mianyang, China). Ethyl acetate (AR) and Dimethyl sulfoxide (AR) were purchased from Aladdin (Shanghai, China).

Preparation of B and B@F

The twofold solvent procedure was used to produce the B coated with F14, which was referred to as B@F. On the one hand, ethyl acetate can dissolve F14, whereas DMSO cannot. On the other hand, ethyl acetate and DMSO are fully miscible in all proportions. As a result, ethyl acetate (solvent) and DMSO (anti-solvent) together form a dual-solvent system, which serves as the foundation of the twofold solvent process. At first, F14 was fully dissolved in 60 g of ethyl acetate with the use of magnetic stirring. Next, B was combined with the previously produced F14 solution using ultrasonic dispersion for 1 hour and magnetic stirring for 2 hours at room temperature. A solution with a uniform composition was produced. The mass ratio of F14 to B was selected as 1:5 based on the oxide layer content of B being around 10 wt.% (obtained by ICP-OES and XPS analysis) and the fluorine content of F14 being approximately 53 wt.% (calculated by its molecular formula: $m_F/m_{C_5F_7Cl_2H}$). This decision was made in accordance with the equation $B_2O_3(l) + CF(s) \rightarrow BF_3(g) + CO(g) + C(s)$. Subsequently, 30 g of DMSO were blended into the precursor solution and subjected to magnetic stirring for 1 hour. Ultimately, adjusting the temperature to

40 °C and opening the fume hood facilitates the evaporation of ethyl acetate. After 2 hours, B@F was acquired. To eliminate the impact of preparation processes on the properties, the B without F14 coated, referred to as B, was additionally subjected to treatment using the twofold solvent approach.

Preparation of B/B_2O_3 components

7.0 g of B_2O_3 was dissolved in 100 mL of deionized water, then 17.6 g of amorphous B powder was added and stirred for 1 h. The obtained dispersion was placed in a vacuum oven and dried for 12 h to remove water.

Heat-treated processes

Heat-treated samples are acquired by subjecting them to a controlled environment inside a muffle furnace. More precisely, a certain quantity of a sample was accumulated in a powdered form inside a corundum crucible located within the muffle furnace. The initial temperature of all heat-treated samples was set at 200 °C. The temperature was then increased to the desired temperature at a heating rate of 10 °C•min^{-1} and maintained for 15 minutes. Subsequently, the samples were allowed to cool naturally until the temperature reached 200 °C before being removed. The target temperatures were determined by considering the melting temperature of boron oxide (450 °C) and the reaction temperature of B in air (~800 °C). The selected temperatures were 500 °C, 600 °C, 700 °C, 800 °C, and 900 °C, respectively.

Preparation of B_6O

Elemental B and B_2O_3 were mixed in stoichiometric proportions according to the reaction equation: $16B(s) + B_2O_3(s, l) \rightarrow 3B_6O(s, l)$. The resulting B/$B_2O_3$ mixture was then placed in a tube furnace and calcined at 1400 °C for 12 hours under an argon atmosphere with a purity of 99.99%.

Characterizations. The morphology was characterized by scanning electron microscopy (FE-SEM, ZIESS, Sigma HD, Germany) at an accelerating voltage of 5 kV. The crystal compositions of the samples were investigated by X-ray diffraction (XRD, Bruker, D8 DISCOVER, Germany) in the range of 2θ: 5° to 40°. The chemical composition and elemental state near-surface region were measured by X-ray photoelectron spectroscopy (XPS, Thermo Scientific, K-Alpha, America) and Fourier Transform Infrared Spectrometer (FTIR, Bruker, VERTEX 70, Germany).

TEM images were collected by using a Talos F200S G2 electron microscope operated at an acceleration voltage of 300 kV. Fresh samples were dispersed ultrasonically, dropped, and dried on a copper grid with lacy support films.

The thermal reaction processes were analyzed by a simultaneous thermal analyzer (TG-DSC, NETZSCH, STA449F5, Germany). Specifically, it was carried out by placing 2 mg sample into a corundum crucible (70 mL) in an air atmosphere (flow rate of 50 mL•min^{-1}) and heating from 50 °C to 900 °C at a heating rate of 10 °C•min^{-1}.

The flame structures underwent examination through the ignition-burning test. A 25 mg sample was placed on the platform, with a Ni-Cr wire (0.4 mm in diameter and 10 cm in length) positioned beneath the samples. The wire was quickly heated to the melting point of Ni-Cr using a custom-built DC current. The entire ignition process was captured using a high-speed camera (UX50, Japan) operating at 500 frames per second. The reaction efficiencies were further characterized by the combustion heat measurements (ZDHW-8E, China). 200 mg of powder were placed into a 330 mL closed boom and ignited by DC power supply in an oxygen atmosphere at 1 MPa, 2 MPa, and 3 MPa, respectively. Each sample underwent three tests to calculate the average value for the combustion heat. The constant volume explosive container system was used to characterize the reaction rates. The pressure-time curve was derived from a closed bomb test. The closed bomb was composed of a pressure cell (330 ml), a pressure sensor (PC290-ACAEFA1A, GAILIN), an oscilloscope, and a power supply. About 200 mg of powder samples were placed into a 5 ml crucible situated within the pressure cell, and ignited using a Ni-Cr wire embedded beneath the samples (with a diameter of 0.4 mm and a length of 10 cm). Before ignition, 1 MPa of oxygen was introduced into the closed bomb. The specific experimental setup is detailed in previous work[30]. A laser ignition device (wavelength was 10.6μm, the focused spot was 4.5 mm) was used to characterize the ignition delay time. 50 mg samples were lit using a laser with a power output of 15/30/45/60 W and an irradiation duration of 1000 milliseconds. The ignition and combustion process were captured by a high-speed camera operating at 1000 frames per second. Each sample underwent five tests to compute the average value for the ignition delay time. The specific experimental procedure and setup are detailed in previous work[31].

Statistics and reproducibility. All tests were conducted using the same experimental setup under identical conditions, with multiple measurements. Each statistical dataset was obtained from three parallel tests, while the ignition delay time was measured five times in parallel.

Data availability

The authors declare that the data supporting the findings of this study are available within the paper and its Supplementary Information files. The raw data files generated over the course of this study are available from the corresponding authors upon request. Source data are provided with this paper.

References

1. Zhang, Z., Penev, E. S. & Yakobson, B. I. Two-dimensional boron: structures, properties and applications. *Chem. Soc. Rev.* **46**, 6746–6763 (2017).
2. Liu, J., Wang, C., Liang, T. & Lai, W. Interaction of boron with graphite: a van der waals density functional study. *Appl. Surf. Sci.* **379**, 402–410 (2016).
3. Grams, R. J. et al The rise of boron-containing compounds: advancements in synthesis, medicinal chemistry, and emerging pharmacology. *Chem. Rev.* 2024.
4. Shao, P. et al. Heterogeneous activation of peroxymonosulfate by amorphous boron for degradation of Bisphenol S. *J. Hazard. Mater.* **322**, 532–539 (2017).
5. Longwitz, L., Leveson-Gower, R. B., Rozeboom, H. J., Thunnissen, A.-M. W. H. & Roelfes, G. Boron catalysis in a designer enzyme. *Nature* **629**, 824–829 (2024).
6. Zhan, C., Zhang, P., Dai, S. & Jiang, D. Boron Supercapacitors. *ACS Energy Lett.* **1**, 1241–1246 (2016).
7. Liu, W. Light-induced activation of boron doping in hydrogenated amorphous silicon for over 25% efficiency silicon solar cells. *Nat. Energy* **7**, (2022).
8. Ding, Z. et al. Effects of boron addition on the high temperature oxidation of MoSi2 alloys. *Scr. Mater.* **234**, 115580 (2023).
9. Buijnsters, J. G. et al. Effect of boron doping on the wear behavior of the growth and nucleation surfaces of micro- and nanocrystalline diamond films. *ACS Appl. Mater. Interfaces* **8**, 26381–26391 (2016).
10. Pang, W.-Q. et al. Boron-Based Composite Energetic Materials (B-CEMs): preparation, combustion and applications. *Prog. Energy Combust. Sci.* **93**, 101038 (2022).
11. Dreizin, E. L. Metal-based reactive nanomaterials. *Prog. Energy Combust. Sci.* **35**, 141–167 (2009).
12. Sundaram, D. Metal-based nanoenergetic materials: synthesis, properties, and applications. *Prog. Energy Combust. Sci*. https://doi.org/10.1016/j.pecs.2017.02.002 2017.

13. Yan, Q.-L. Catalytic effects of nano additives on decomposition and combustion of RDX-, HMX-, and AP-based energetic compositions. *Prog. Energy Combust. Sci.* https://doi.org/10.1016/j.pecs.2016.08.002 2016.
14. King, M. K. Ignition and combustion of boron particles and clouds. *J. Spacecr. Rockets* **19**, 294–306 (1982).
15. He, W., Liu, P., He, G., Gozin, M. & Yan, Q. Highly Reactive Metastable Intermixed Composites (MICs): preparation and characterization. *Adv. Mater.* **30**, 1706293 (2018).
16. Meinko¨Hn, D. Boron particle ignition and the Marangoni effect. *Combust. Sci. Technol.* **176**, 1493–1536 (2004).
17. Meinköhn, D. Metal-particle ignition and oxide-layer instability. *Combust. Explos. Shock Waves* **42**, 158–169 (2006).
18. Wu, X. & Wei, Z. Multiphase ignition and combustion model and its characteristics of boron particles based on dynamic experimental phenomena. *Combust. Flame* **265**, 113445 (2024).
19. King, M. K. Boron ignition and combustion in air-augmented rocket afterburners. *Combust. Sci. Technol.* **5**, 155–164 (1972).
20. King, M. K. Boron particle ignition in hot gas streams. *Combust. Sci. Technol.* **8**, 255–273 (1973).
21. Li, S. C. & Williams, F. A. Ignition and combustion of boron in wet and dry atmospheres. *Symp. Int. Combust.* **23**, 1147–1154 (1991).
22. Dreizin, E. L. Effect of phase changes on metal-particle combustion processes. *Combust. Explos. Shock Waves* **39**, 681–693 (2003).
23. Glassman, I., Williams, F. A. & Antaki, P. A Physical and chemical interpretation of boron particle combustion. *Symp. Int. Combust.* **20**, 2057–2064 (1985).
24. Yeh, C. L., Kuo, K. K., Klimkiewicz, M. & Brown, P. W. Environmental scanning electron microscopy studies of diffusion mechanism of boron particle combustion. *Scanning* **19**, 114–118 (1997).
25. Yeh, C. L. & Kuo, K. K. Ignition and combustion of boron particles. *Prog. Energy Combust. Sci.* **22**, 511–541 (1996).
26. Liang, D., Liu, J., Zhou, Y., Zhou, J. & Cen, K. Ignition and combustion characteristics of molded amorphous boron under different oxygen pressures. *Acta Astronaut* **138**, 118–128 (2017).
27. Song, Q. et al. Laser ignition and combustion characteristics of micro- and nano-sized boron under different atmospheres and pressures. *Combust. Flame* **230**, 111420 (2021).
28. Wang, D. et al. Dual-core–shell structure B@LiF@AP with multi-effect synergies to improve processibility and energy release characteristics of B. *J. Mater. Chem. A* **11**, 1351–1360 (2023).
29. Qin, Y. et al. Energetic properties of core–shell B@PVDF/AP composite micro-units prepared by electrostatic spraying technology. *Chem. Eng. J.* **496**, 154379 (2024).
30. Wang, J. et al. Synergistic reaction of spherical B/Al/PTFE fuel prepared by confinement-emulsion-templated strategy to achieve high energy and reactivity. *Combust. Flame* **259**, 113113 (2024).
31. Wang, J. et al. Surface engineering boron/graphite fluoride composite with enhanced ignition and combustion performances. *Fuel* **323**, 124374 (2022).
32. Weismiller, M. R., van Duin, A. C. T., Lee, J. & Yetter, R. A. ReaxFF reactive force field development and applications for molecular dynamics simulations of ammonia borane dehydrogenation and combustion. *J. Phys. Chem. A* **114**, 5485–5492 (2010).
33. Wang, J., Zhu, B. & Sun, Y. Microscopic mechanism of α-rhombic crystal boron nanocluster oxidation in oxygen. *Fuel* **310**, 122448 (2022).
34. Feng, M. Atomistic insights into two-stage combustion of a single boron nanoparticle via reactive molecular dynamics. *Fuel* **375**, 132628 (2024).
35. Higashi, I., Kobayashi, M., Bernhard, J., Brodhag, C. & Thévenot, F. Crystal structure of B6O. *AIP Conf. Proc.* **231**, 201–204 (1991).

Acknowledgements

J.W., K.Z., X.Z., Y.M., F.N., J.C., H.G., and J.W. were supported by the National Natural Science Foundation of China (T2222027 (J.W.), T2225027 (H.G.), and 12202416 (J.C.)). Thanks to SiChuan Hbst. Co., Ltd for combustion performance testing. We thank the Analysis and Testing Center of Southwest University of Science and Technology for providing SEM, the Beijing National Center for Electron Microscopy and the Laboratory of Advanced Materials of Tsinghua University for their help in TEM observations.

Author contributions

Jian W. prepared samples, carried out the heat treatment experiment and combustion reaction performance test, analyzed the experimental data, and wrote the initial manuscript. Jun W. provided the initial inspiration for the project, conceived the project, planned and carried out the experiments, wrote the initial manuscript, and revised the manuscript; K.Z. carried out a molecular dynamics simulation and analyzed the simulation results. X.Z. and Y.M. assisted in the preparation of the sample and carried out some heat treatment experiments and SEM testing. F.N. and J.C. participated in the discussion of the experiment and assisted in the analysis. H.G. planned the experiments and wrote and revised the manuscript. All authors contributed to the discussion and revision of the paper.

Competing interests

The authors declare no competing interests.

Additional information

Supplementary information The online version contains supplementary material available at https://doi.org/10.1038/s41467-025-64797-x.

Correspondence and requests for materials should be addressed to Huiyang Gou or Jun Wang.

Peer review information *Nature Communications* thanks Bin Liu and the other anonymous reviewer(s) for their contribution to the peer review of this work. A peer review file is available.